Enhanced intermediate-temperature CO[subscript 2] splitting using nonstoichiometric ceria and ceria–zirconia

Citation: .Zhao, Zhenlong, et al. "Enhanced Intermediate-Temperature CO[subscript 2] Splitting Using Nonstoichiometric Ceria and Ceria–Zirconia." Physical Chemistry Chemical Physics, vol. 19, no. 37, 2017, pp. 25774–85.

As Published: http://dx.doi.org/10.1039/C7CP04789D

Publisher: Royal Society of Chemistry (RSC)

Persistent URL: http://hdl.handle.net/1721.1/118852

Version: Author's final manuscript: final author's manuscript post peer review, without publisher's formatting or copy editing

PCCP

PAPER

View Article Online
View Journal

Cite this: DOI: 10.1039/c7cp04789d

Enhanced intermediate-temperature CO_2 splitting using nonstoichiometric ceria and ceria–zirconia†

Zhenlong Zhao, [a] Mruthunjaya Uddi,[b] Nikolai Tsvetkov,‡[c] Bilge Yildiz*[c] and Ahmed F. Ghoniem*[a]

CO_2 splitting *via* thermo-chemical or reactive redox has emerged as a novel and promising carbon-neutral energy solution. Its performance depends critically on the properties of the oxygen carriers (OC). Ceria is recognized as one of the most promising OC candidates, because of its fast chemistry, high ionic diffusivity, and large oxygen storage capacity. The fundamental surface ion-incorporation pathways, along with the role of surface defects and the adsorbates remain largely unknown. This study presents a detailed kinetics study of CO_2 splitting using CeO_2 and $Ce_{0.5}Zr_{0.5}O_2$ (CZO) in the temperature range 600–900 °C. Given our interest in fuel-assisted reduction, we limit our study to relatively lower temperatures to avoid excessive sintering and the need for high temperature heat. Compared to what has been reported previously, we observe higher splitting kinetics, resulting from the utilization of fine particles and well-controlled experiments which ensure a surface-limited-process. The peak rates with CZO are 85.9 μmole g^{-1} s^{-1} at 900 °C and 61.2 μmole g^{-1} s^{-1} at 700 °C, and those of CeO_2 are 70.6 μmole g^{-1} s^{-1} and 28.9 μmole g^{-1} s^{-1}. Kinetic models are developed to describe the ion incorporation dynamics, with consideration of CO_2 activation and the charge transfer reactions. CO_2 activation energy is found to be −120 kJ $mole^{-1}$ for CZO, half of that for CeO_2, while CO desorption energetics is analogous between the two samples with a value of ~160 kJ $mole^{-1}$. The charge-transfer process is found to be the rate-limiting step for CO_2 splitting. The evolution of CO_3^{2-} with surface Ce^{3+} is examined based on the modeled kinetics. We show that the concentration of CO_3^{2-} varies with Ce^{3+} in a linear-flattened-decay pattern, resulting from a mismatch between the kinetics of the two reactions. Our study provides new insights into the significant role of surface defects and adsorbates in determining the splitting kinetics.

Received 16th July 2017,
Accepted 24th August 2017

DOI: 10.1039/c7cp04789d

rsc.li/pccp

Introduction and background

CO_2 emission from fossil fuel combustion is a major contributor to global warming. The currently proposed approach to reduce anthropogenic CO_2 emissions from fossil fuels is carbon capture and sequestration (CCS), in which CO_2 is separated from the flue gases, liquefied, and injected in geological formations. Significant challenges remain with CCS, mostly in process economics, safety, and long-term stability. Developing alternative approaches, such as CO_2 splitting technologies, is thus motivated by energy needs and environmental concerns. Among various options, thermo-chemical CO_2 splitting has attracted significant interest, inspired by the thermo-chemical H_2O splitting technology.[1–3] Using oxygen-deficient metal oxide (commonly referred to as oxygen carrier, OC), CO_2 is dissociated into CO *via*:

Oxidation:

$$CO_2(g) + V_O^{\bullet\bullet} + 2e' \rightleftharpoons CO(g) + O_O^{\times} \quad (1)$$

where $V_O^{\bullet\bullet}$ denotes a surface oxygen vacancy and $O_O^{\times}$ is an oxygen ion on a normal site. The surface defect acts as an oxygen sink, enabling CO_2 dissociation at lower temperatures (<1000 °C, in contrast to the direct gas-phase thermolysis reaction). Oxidation is followed by a reduction step, where the defects are regenerated:

Thermal reduction:

$$O_O^{\times} \rightleftharpoons \frac{1}{2}O_2(g) + V_O^{\bullet\bullet} + 2e' \quad (2)$$

Fuel reduction:

$$O_O^{\times} + CH_4(g) \rightleftharpoons CO(g) + 2H_2(g) + V_O^{\bullet\bullet} + 2e' \quad (3)$$

Here the oxygen removal step is achieved by either heating the metal oxides using, *e.g.*, concentrated solar irradiation (eqn (2),

[a] Department of Mechanical Engineering, Massachusetts Institute of Technology, 77 Massachusetts Avenue, Cambridge, MA 02139-4307, USA. E-mail: ghoniem@mit.edu
[b] Department of Mechanical Engineering, University of Alabama, Tuscaloosa, AL 35487, USA
[c] Department of Nuclear Science & Engineering, and Department of Materials Science & Engineering, Massachusetts Institute of Technology, 77 Massachusetts Avenue, Cambridge, MA 02139-4307, USA. E-mail: byildiz@mit.edu

† Electronic supplementary information (ESI) available. See DOI: 10.1039/c7cp04789d

‡ Current address: Graduate School of Energy, Environment, Water, and Sustainability, Korea Advanced Institute of Science and Technology, Daejeon 305-701, Korea.

e.g., thermo-chemical CO_2 splitting), or reducing the OC using a fuel (eqn (3), or reactive chemical-looping CO_2 splitting). The net reaction combining the reduction and oxidation (redox) steps becomes CO_2 intermediate temperature thermolysis, *i.e.*, $CO_2 \rightleftharpoons CO + 1/2O_2$, or dry reforming, $CO_2 + CH_4 \rightleftharpoons 2CO + 2H_2$. The OC remains intact as it dissociates CO_2 through this two-step process. The transfer of oxygen between the redox steps exploits the oxygen non-stoichiometric capacity of the metal oxide by mediating the oxygen fugacity in the reactive environment, either by heating or flowing a fuel, which drives the two-way ionic exchange between the gas and the solid. Promising results have been demonstrated for the efficient production of CO/syngas,[2,4–6] which are key precursors to the synthesis of liquid fuel and commodity chemicals. Although exhibiting remarkable promise, major challenges exist for the thermal reduction method (eqn (2)), mostly resulting from the need for expensive high quality heat and a large temperature swing which can render the process less efficient and less durable. On the other hand, using fuel as a reducing agent (eqn (3)) in the CO_2 splitting process may benefit from the abundance and low price of natural gas, and thus offer a simple and promising solution for CO_2 reduction. The use of fuel enables faster reduction at a lower temperature (<900 °C) with enhanced oxygen deficiency in the solid, and thus a larger oxygen carrying capacity at a given temperature. The temperature swing is thus replaced by an isothermal operation with reduced costs and improved long-term stability.

Among various OC options for CO_2 splitting, ceria has emerged as one of the most promising candidates, owing to its rapid surface chemistry and fast ionic conductivity.[2,7,8] The large non-stoichiometric capacity achieved at elevated temperature allows it to effectively exchange oxygen while adjusting to the redox environment.[9,10] A variety of experiments have demonstrated the feasibility of CO_2 splitting using ceria and ceria-based materials,[2–4,7,11–19] and a brief comparison is shown in Table 1. Extensive efforts have been made lately to extend the redox properties of ceria towards lower temperatures for improved system efficiency.[15,20,21] The addition of an undersized dopant, such as Zr^{4+}, induces structural distortion,[22] leading to enhanced oxygen mobility[23] and lower defect formation energy[24] with improved long-term structural stability.[25,26] A recent kinetics study[27] demonstrates that doping with 50 mol% Zr in ceria lowers the defect formation enthalpy by over 40%, resulting in dramatic improvement of the redox kinetics at 600 °C. These redox properties of ceria and ceria–zirconia have been widely exploited in thermo-chemical water splitting studies,[27,28] as well as many other applications,[7,8,20,22,28–31] including three-way catalysis, water-gas shift, solid oxide fuel cells, electrolyzers, methane reforming, *etc.*

CO oxidation on ceria has been extensively investigated over the past few decades, with focus on its oxygen storage capacity,[23,32] adsorbates,[33,34] and spillover pathways between ceria and supported metal catalysts.[35,36] CO_2 reactivity, however, is not well understood, and it is usually treated as the ''reverse'' of the CO oxidation reaction.[37] Recently, there has been an increasing effort towards a better understanding of CO_2 activation and the important role of the surface defects,[38–42] owing to the rising interest in fuel cells, electrolyzers, and thermo-chemical CO_2 splitting. Advanced *in situ* techniques, such as X-ray adsorption spectroscopy (XAS),[43] and X-ray photoemission spectroscopy (XPS),[44,45] have been applied to probe the structural dynamics and the adsorbate–vacancy interactions under a CO_2/CO environment. Density functional studies have examined the preferable sites and surface orientations for CO_2 activation and evaluated the importance of surface vacancies on the formation of chemisorbed carbonates, CO_3^{2-}.[37,40,46–48] Most recently, a few studies have

Table 1 Reported total and peak CO production rates using ceria or ceria–zirconia as OC

Temp. (°C) (Red/Ox)	Oxygen carrier (OC)	Tot. CO (μmole g^{-1})	Peak rate[g] (μmole g^{-1} s^{-1})	Feed CO_2 (%)	Reducer	OC surface area (m^2 g^{-1})	Ref.
1500/800	CeO_2	280	6.8	50	Thermal	—	2[a]
1400/1000	CeO_2	105	—	50	Thermal	—	11
	$Ce_{0.75}Zr_{0.25}O_2$	241					
1400/1000	CeO_2	100	—	50	Thermal	—	12[b]
	$Ce_{0.75}Zr_{0.25}O_2$	242					
	$Ce_{0.9}Zr_{0.1}O_2$	130					
1600/1000	CeO_2	219	1.9	60	Thermal	6.0	3[c]
1527/827	CeO_2	89	0.4	8.3	Thermal	—	4[d]
1200/850	CeO_2	37	4.0	25	Thermal	3.95	13
1500/800	CeO_2	180	1.6	38.5	Thermal	0.095	14
1400/800	CeO_2	180	45	100	Thermal	1.7	15
	$Ce_{0.75}Zr_{0.25}O_2$	430	1.5			2.1	
1500/1500	CeO_2	90	2.5	100	Thermal	—	19[e]
1400/1000	CeO_2	55	—	100	Thermal	—	16
	$Ce_{0.5}Zr_{0.5}O_2$	272					
1100/500	CeO_2	600	8	0.5–40	H_2	—	17[f]
827/827	CeO_2	934	24.8	4	H_2	10.2	18
900/900	CeO_2	1013 ± 120	70.6 ± 1.2	14.3	H_2	4.07	This study
700/700		186 ± 80	28.9 ± 1.0				
900/900	$Ce_{0.5}Zr_{0.5}O_2$	827 ± 122	85.9 ± 4.3	14.3	H_2	22.96	This study
700/700		555 ± 108	61.2 ± 3.6				

[a] Data from Fig. 3. [b] CO production rates at the third cycle. [c] Data from Fig. 6 based on ceria felt. [d] Data from Fig. 2, H_2O (47%) is also fed. [e] Data from Fig. 9. [f] Peak rate is from the highest rate in Fig. 4, total production corresponds to $\delta = 0.1$. [g] Conversion of CO production unit from mL g^{-1} to μmole g^{-1} utilizes ideal-gas law at standard temperature and pressure (25 °C 1 atm).

examined the redox kinetics following an equilibrium approach[49] or empirical kinetics models,[14,15,17] and a general consensus has been reached regarding the critical role of the surface chemistry on CO_2 splitting.[17] Despite the efforts and promising proof-of-principle in lab-scale prototypes, investigation on the fundamental surface redox pathways requires further attention.[7,35] The details involved in the interactions of mobile ions, and electrons between the bulk and the surface, along with the gaseous reactants, adsorbates and electrostatic fields are complex; a thorough understanding of these mechanisms is technologically important for the design and optimization of the CO_2 splitting process.

In this work, we investigate the intermediate-temperature CO_2 splitting mechanisms of CeO_2 and $Ce_{0.5}Zr_{0.5}O_2$ (CZO), with emphasis on the surface ion-incorporation kinetic pathway. Isothermal redox cycles of CeO_2 and CZO nano-powder are carried out in a button cell reactor in the temperature range 600–900 °C. H_2 is used as a surrogate fuel in the reduction step to reconstruct the highly oxygen-deficient non-stoichiometry, and to study the fundamentals of ceria redox reactions associated with surface ion-incorporation and defect transport processes. The use of fuel in the reduction step enhances oxygen deficiency, leading to much faster splitting kinetics at low temperature (~700 °C); therefore, the temperature in the experiment is capped at 900 °C. In real applications, H_2 could be used, but it is better if hydrocarbons, most likely CH_4, could be used during the reduction step to produce syngas. The kinetics and the oxygen-ion incorporation pathway for the CO_2 splitting process are probed on the basis of the previously derived defect equilibria and mechanism framework from the H_2O splitting studies.[27,28] The mechanism consists of a series of intermediate steps: adsorption/dissociation of gaseous reactants, charge transfer on the surface, and the bulk-to-surface transport. Based on the kinetic models, rate-limiting mechanisms are identified, and insights are gained on the role of surface defects and interactions with adsorbates. The derived CO_2 splitting pathway serves as a baseline for developing a detailed reaction mechanism with complex hydrocarbons as reducing agent.[50] The knowledge of the redox kinetics data also provides important guidance for the design and optimization of oxygen carriers for related applications.

Experimental setup and theoretical methods

Redox kinetics measurement

CeO_2 and $Ce_{0.5}Zr_{0.5}O_2$ nanopowder from Sigma Aldrich are used for the kinetics study (see ESI† for sample properties and characterization). Fresh samples contain very fine particles with the size less than 50 nm. After initial thermal and redox treatment, CeO_2 particles sinter into larger grains (~200 nm, see Table S1 and Fig. S1, ESI†). Compared to CeO_2, the size enlargement for CZO is less significant (~50 nm), resulting from the enhanced structural stability with the addition of Zr. Interesting, the variations in the measured kinetics of CeO_2 and CZO are rather small except for a few initial (<5) cycles, indicating that the morphological relaxation most likely results from the sintering effect during the heating-up and initial redox cycling; hence, the kinetics analysis focuses on the cyclic equilibrated states. The redox kinetics is measured in a button-cell fixed-bed reactor, which consists of a gas delivery system, a control unit, a central quartz reactor tube, and a real-time flue gas analysis system using an on-line quadrupole mass-spectrometer (QMS). The central quartz tube is positioned inside a split tube furnace that provides an isothermal environment up to 1100 °C. A detailed description of the system can be found in ref. 28. During the kinetics study, a minute amount of CeO_2 (100 mg) or CZO (50 mg) powder is embedded in quartz wool and placed at the bottom of the outer quartz tube. The sample undergoes redox cycles with argon as the purging gas flowing in between. The total flow rate into the reactor is fixed at 350 sccm, corresponding to a gas residence time of less than 300 ms through the dispersed sample. Oxidation is performed using a gas mixture of carbon dioxide (14.3 mol%) and argon. H_2 is used as the reducing gas instead of CH_4 or CO to rule out coke formation and its subsequent contribution towards H_2 generation through the steam-carbon reaction. The total flow for reduction is maintained constant at 350 sccm with a H_2 mole fraction of 14.3 mol% (Ar balance). The oxidation and reduction times are fixed at 2 min each with 5 min Ar purging in between. A supplemental 2 min oxidation with 0.5% O_2 (Ar balance) is used after the CO_2 splitting step to ensure a complete regeneration of stoichiometry. Both samples are pre-treated at 1000 °C to reach periodic stationary states. Particle enlargement is observed during the early cycles (see ESI† for details). After pretreatment, the measurements are taken from 900 °C down to 600 °C with a step of 100 °C. Each operating condition is repeated at least three times, and results are averaged to reduce the noise.

CO_2 surface chemistry

The CO_2 splitting reaction on the surface is modeled using a two-step mechanism (Fig. 1),[46,47,51–55] with the corresponding mass action rate expressions as:

$$\mathrm{R1}: \mathrm{CO_2(g)} + \mathrm{V_O^{\bullet\bullet}(s)} + \mathrm{O_O^{\times}(s)} \underset{k_{1,\mathrm{b}}}{\overset{k_{1,\mathrm{f}}}{\rightleftharpoons}} \mathrm{(CO_3)_O^{\bullet\bullet}(s)} \tag{4}$$

$$r_1 = k_{1,\mathrm{f}} p_{\mathrm{CO_2}} \left[\mathrm{V_O^{\bullet\bullet}}\right]_\mathrm{s} \left[\mathrm{O_O^{\times}}\right]_\mathrm{s} - k_{1,\mathrm{b}} \left[\mathrm{(CO_3)_O^{\bullet\bullet}}\right]_\mathrm{s} \tag{5}$$

$$\mathrm{R2}: \mathrm{(CO_3)_O^{\bullet\bullet}(s)} + 2\mathrm{Ce_{Ce}^{'}(s)} \underset{k_{2,\mathrm{b}}}{\overset{k_{2,\mathrm{f}}}{\rightleftharpoons}} \mathrm{CO(g)} + 2\mathrm{Ce_{Ce}^{\times}(s)} + 2\mathrm{O_O^{\times}(s)} \tag{6}$$

$$r_2 = k_{2,\mathrm{f}} \left[\mathrm{(CO_3)_O^{\bullet\bullet}}\right] \left[\mathrm{Ce_{Ce}^{'}}\right]^2 - k_{2,\mathrm{b}} p_{\mathrm{CO}} \left[\mathrm{O_O^{\times}}\right]^2 \left[\mathrm{Ce_{Ce}^{\times}}\right]^2 \tag{7}$$

$(CO_3)_O^{\bullet\bullet}$ (or equivalently CO_3^{2-}) is a surface carbonate group formed near the vacancy. $k_{i,\mathrm{f}}$, $k_{i,\mathrm{b}}$, denotes the rate coefficients (unit, s^{-1}), following the Arrhenius expression, $k = k_0 \exp(-E/RT)$. The surface reactions are assumed to occur only within the first unit cell layer on the surface, and the s in parenthesis emphasizes this assumption. R1 describes the chemisorption and activation processes of CO_2, which is then followed by the charge transfer

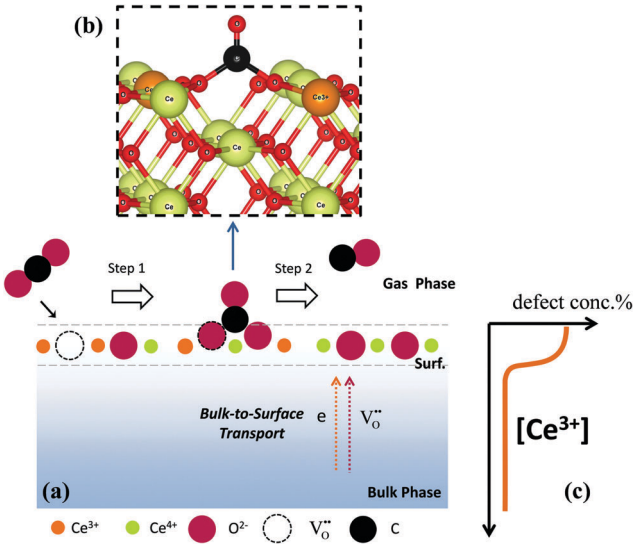

Fig. 1 (a) Schematics of the CO_2 splitting pathway. The ion-incorporation surface process comprises the adsorption and activation of CO_2 forming carbonates, CO_3^{2-} (R1); charge transfer, association and desorption of CO (R2). The heterogeneous chemistry is linked to the bulk phase *via* the bulk-to-surface transport of the electron defect, e, and the oxygen vacancy defect, $V_O^{\bullet\bullet}$. (b) Side view of CO_3^{2-} on the O-bridge site of the (110) surface. (c) Schematics of the surface enrichment of Ce^{3+} relative to the bulk.

and desorption step (R2). R1 is energetically favored on the oxygen-deficient surface,[40,51] while R2 is an endothermic process, hence most likely limiting the overall CO_2 splitting process.[44,55] This has also been shown for H_2O splitting, both experimentally[28,56] and computationally.[28,40,57,58]

It is generally agreed that the adsorption and activation of CO_2/CO over ceria favors the more active surfaces, *e.g.*, (110), (100), *etc.*, as opposed to (111) for H_2O splitting.[40] Density functional studies[46,47,51] identified the O-bridge on (110) surface near the vacancy (see Fig. 1(b)) as one of the most stable sites for the CO_2/CO activation process: upon adsorption, a carbonate CO_3^{2-} is formed, likely bent and tilted, with two electrons localized in the nearest neighbor (or next nearest neighbor) cation sites and the two surface O ions slightly pulled away from the surface. The exact shape of the adsorbate and the elementary pathway leading to its formation, however, still remain a matter of debate. Other chemisorbates, such as CO_2, CO_2^-, unidentate CO_3^{2-}, *etc.*, are also possible,[40] and their formation depends on the types of vacancies,[37] surface orientation,[51,52] sites and dopant,[47,59] coverage,[44,48] and the sequence of the charge transfer,[37,44] *etc.* The addition of Zr^{4+} does not alter the electronic structure, thus maintaining an analogous splitting pathway as with CeO_2; however, subtle differences exist on the electron localization patterns resulting from fewer available Ce^{4+} in CZO.[47] Identifying the detailed elementary steps and precisely quantifying the contribution from each factor are not the focus of this study. Rather, we model the CO_2 splitting kinetics with the two-step mechanism (eqn (4)–(7)) *via* the formation of the surface carbonate intermediate, thus providing an adequate description of the surface electro-chemical process without over-fitting.

At equilibrium, r_1 and r_2 are zero. This leads to the definition of the corresponding equilibrium constants K_1 and K_2. Combining R1 and R2 yields the overall surface equilibrium as:

$$V_O^{\bullet\bullet}(s) + 2Ce_{Ce}'(s) + CO_2(g) \overset{K_s}{\rightleftharpoons} O_O^{\times}(s) + 2Ce_{Ce}^{\times}(s) + CO(g) \quad (8)$$

which is related to the bulk-phase equilibrium *via* $K_s = (K_b K_{CO_2} K_T)^{-1}$ (see ESI† for detailed derivation). Here, K_b, K_{CO_2}, and K_T, are the equilibrium constants of the defect formation reaction, CO_2 formation reaction, and defect transport equilibrium, respectively:

Defect formation:

$$O_O^{\times} + 2Ce_{Ce}^{\times} \overset{K_b}{\rightleftharpoons} V_O^{\bullet\bullet} + 2Ce_{Ce}' + \frac{1}{2}O_2(g) \quad (9)$$

CO_2 formation:

$$CO(g) + \frac{1}{2}O_2(g) \overset{K_{CO_2}}{\rightleftharpoons} CO_2(g) \quad (10)$$

Defect transport:

$$V_O^{\bullet\bullet}(b) - O_O^{\times}(b) + 2Ce_{Ce}'(b) - 2Ce_{Ce}^{\times}(b) \overset{K_T}{\rightleftharpoons} V_O^{\bullet\bullet}(s) - O_O^{\times}(s) + 2Ce_{Ce}'(s) - 2Ce_{Ce}^{\times}(s) \quad (11)$$

From eqn (10), equilibrium oxygen fugacity in the CO_2/CO environment can also be defined, as $p_{O_2} = p_{CO_2}{}^2 \Big/ \left(K_{CO_2} p_{CO}\right)^2$. Coupled with the site conservation and electro-neutrality, the evolution of the surface adsorbate $(CO_3)_O^{\bullet\bullet}$ and the bulk-phase $V_O^{\bullet\bullet}$ can be solved numerically, (see ESI†), and the kinetics parameters can thus be extracted by fitting to the experimental results.

Result and discussion

CO_2 splitting kinetics

Fig. 2 compares the CO_2 splitting kinetics between CeO_2 (solid lines) and CZO (dashed) at 900 °C. For both samples, the process follows a similar pattern: the reactivity spikes with the feed of CO_2, and transits to a slow residual conversion, which eventually ceases near the end of oxidation. The fast conversion at the initial stage is accompanied by a rapid incorporation of O ions into the lattice, as seen in panel (b). As the oxygen vacancy is gradually filled up, the splitting rate slows down quickly and eventually reaches zero. The maximum rate is thus a combined effect from the intake of the gaseous reactant and the consumption of defects. Most of the conversion is completed within 0.5 min, although the oxygen incorporation process continues towards the end.

Despite the significant difference in the stoichiometric composition and particle geometry, similarities are found in the initial defect concentration and splitting kinetics. The analogous oxygen vacancy concentration, determined in the preceding reduction step, is attributed to the oxygen carrying capacity and utilization efficiency: on one hand, CeO_2 possesses twice the available oxygen as compared to $Ce_{0.5}Zr_{0.5}O_2$, since only the CeO_2 portion contributes to oxygen transfer; on the other hand, the addition of Zr^{4+} results in an 40% reduction of the defect

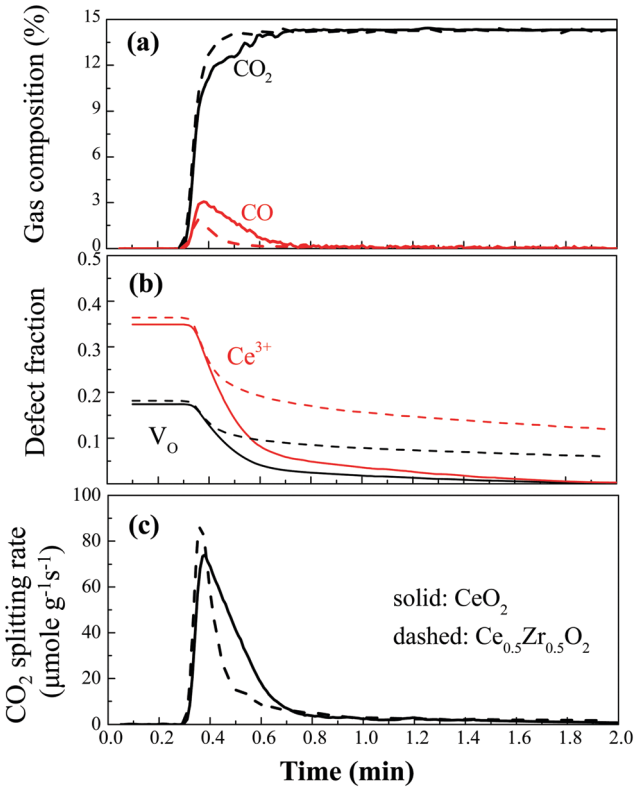

Fig. 2 CO_2 splitting during the oxidation step at 900 °C for 100 mg CeO_2 (solid lines) and 50 mg CZO (dashed lines). (a) Species mole fraction of CO, CO_2; (b) evolution of the bulk defect fraction; (c) the CO_2 splitting rate. The initial defect concentration in panel (b) is taken from the previous reduction cycle (see ESI† for detailed calculation).

formation enthalpy (see ESI,† Table S1), leading to an enhanced activation of lattice oxygen and hence a better utilization (~72%) of its carrying capacity as compared to CeO_2 (~35%).

Given the similarity in the initial oxygen deficiency in both samples but the difference in the surface area (see ESI,† Table S1), one may expect a much faster CO_2 splitting kinetics for CZO, as opposed to the overlapping rate kinetics observed during the initial stage in Fig. 2(a). The similarity in the splitting kinetics originates from the much enhanced charge-transfer rate for CeO_2 at high temperature, resulting from the more pronounced defect segregation and hence higher defect concentration at the surface. As shown in Fig. 3, Ce^{3+} concentration on the surface of CeO_2 is almost twice that of CZO, accounting for over 75% of all available Ce sites on the surface. The highly reduced surface thus leads to a much higher concentration of the activated carbonate in CeO_2 (see modeling results, Fig. 8), which facilitates the charge-transfer reaction (R2). A complete regeneration of CeO_2 stoichiometry is established at the end of oxidation. This is in contrast to CZO, where the rate decays more rapidly, and the conversion ceases around $\delta = 0.05$, where equilibrium is established between oxygen non-stoichiometry and the CO_2/CO environment.[27]

Effect of temperature

Fig. 4 compares the profiles of CO_2 splitting rates as a function of temperature between CeO_2 and CZO. Both CeO_2 and CZO exhibit strong temperature dependence with the rate profile becoming taller and wider at a higher temperature, indicating a high activation barrier associated with the splitting process. The peak rate varies nonlinearly with temperature: a large jump takes place as the temperature is raised over 700 °C for CeO_2 and 600 °C for CZO, but a minor improvement on the peak rate is observed at a higher temperature. The non-linearity is in good accordance with the variation of the initial defect concentrations at the surface, as seen in panels (b) and (d), which rises and flattens at high temperature. Compared to the bulk phase, the vacancy on the surface is significantly higher, and the surface enrichment effect is more pronounced in the case of CeO_2.

The peak rates and the total CO production are compared in Fig. 5. Comparable CO_2 splitting rates are observed at a higher temperature, while more evident improvement is found for CZO at low temperature with twice as fast kinetics at 700 °C, resulting from the enhanced reducibility with Zr and the finer particle structures maintained throughout the redox cycling. The peak rates with CZO are 85.9 μmole g^{-1} s^{-1} at 900 °C and 61.2 μmole g^{-1} s^{-1} at 700 °C, and those of CeO_2 are 70.6 μmole g^{-1} s^{-1} and 28.9 μmole g^{-1} s^{-1}, respectively. Panel (a) also includes the peak rates from the H_2O splitting experiments.[27,28] At high temperature, the rate with H_2O is higher as compared to CO_2 for both cases, while an opposite trend is observed at low temperature with CZO where the CO_2 and H_2O splitting curves cross around 700–800 °C. Compared to H_2O splitting, the CO_2 curve for CZO exhibits weaker temperature dependence, suggesting a lower activation barrier.

Panel (b) compares the overall CO and H_2 yield during the 2 min oxidation step. The splitting yield is strongly dependent on temperature over the entire temperature range, in contrast to the weak temperature dependence observed for the peak rate at high temperature. The H_2O or CO_2 splitting yield matches closely for CeO_2: both oxidation processes completely restore

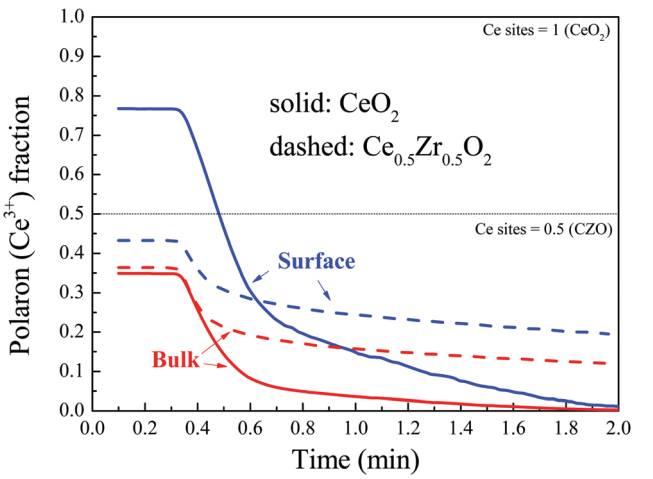

Fig. 3 Comparison of the polaron concentration in the bulk and on the surface for oxidation at 900 °C. Calculation of surface polaron concentration can be found in the ESI,† with the bulk concentration from Fig. 2. The total Ce sites for CeO_2 and CZO are also included for reference. The calculation here assumes $[CO_3^{2-}] = 0$ on the surface.

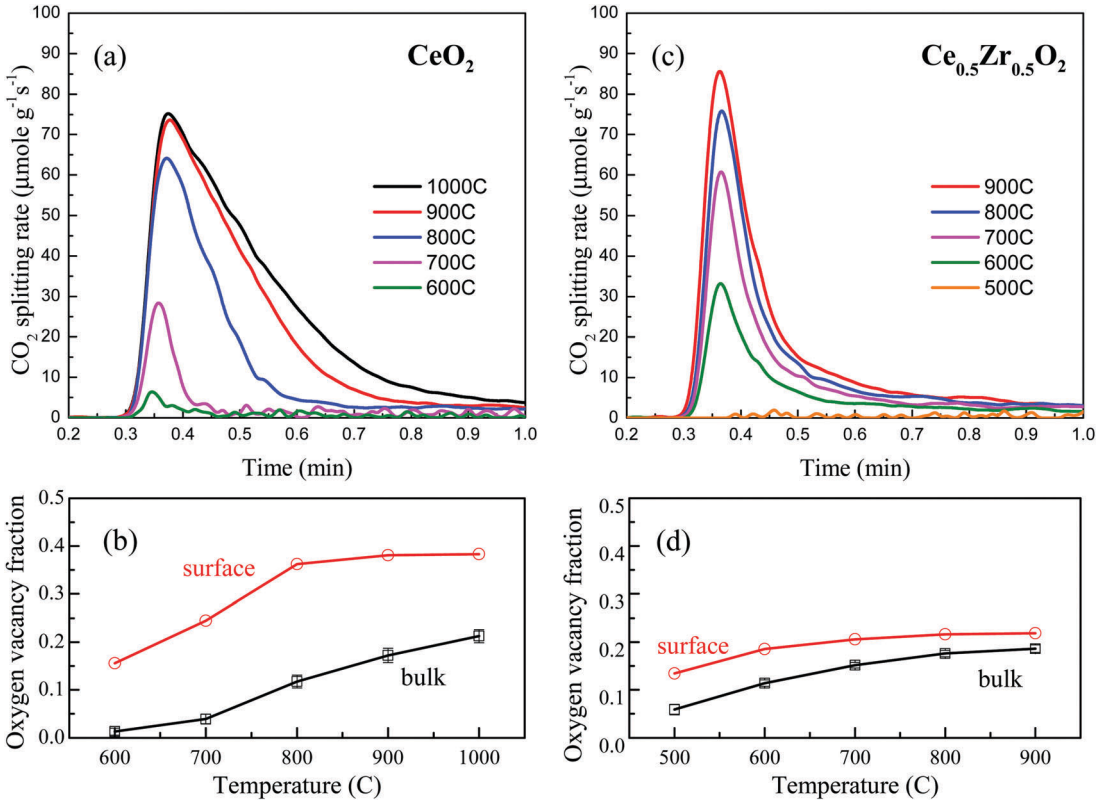

Fig. 4 Comparison of the temperature dependence for the CO_2 splitting rate between (a) CeO_2 and (c) $Ce_{0.5}Zr_{0.5}O_2$. 14.3 mol% CO_2 at 350 sccm is used for oxidation. Reduction occurs at 14.3 mol% H_2 for 2 min at the temperature in accordance with the oxidation step. Panel (b) and (d) show the oxygen vacancy fraction in the bulk (black) and on the surface (red) after the fuel reduction step. The data at 1000 °C for CeO_2 and 500 °C for CZO are also included. The maximum oxygen vacancy is 0.5 for CeO_2 and 0.25 for $Ce_{0.5}Zr_{0.5}O_2$.

the oxygen stoichiometry; therefore, the total evolved H_2 or CO is determined by the non-stoichiometry created during similar reduction steps, as shown in Fig. 4(b). On the other hand, a discrepancy is observed for CZO, where H_2O oxidation prevails at high temperature with the opposite at low temperature. A previous study[27] attributed the insufficient OC regeneration of CZO to the combined effects of the equilibrium constraints and the slow charge-transfer kinetics, with the former more dominant at high temperature and the latter at low temperature. Given the fact that the CO_2/CO environment has a higher equilibrium p_{O_2} above 800 °C as compared to H_2O/H_2, but a lower value at lower temperature (*i.e.*, K_{CO_2} (900 °C) = 1.1 × 10^8 < K_{H_2O}(900 °C) = 1.43 × 10^8, K_{CO_2} (700 °C) = 4.2 × 10^{10} > K_{H_2O}(900 °C) = 2.7 × 10^{10}), one may expect an opposite trend in comparison to Fig. 5(b). Again, the reason is the weaker barrier in CO_2 splitting, as will be shown in Fig. 7 and 9, such that the splitting rate becomes faster with CO_2 at low temperature. Compared to CZO, the splitting yield of H_2 or CO with CeO_2 is generally less over most of the temperature range, with an exception at 900 °C, where the CO yield with CZO is lower, as also evident from Fig. 2(c). The total CO yield for CeO_2 is 1014 μmole g^{-1} s^{-1} at 900 °C, and 186 μmole g^{-1} s^{-1} at 700 °C, corresponding to $\Delta\delta$ of 0.175 and 0.03, respectively, while that for CZO is 827 μmole g^{-1} s^{-1} ($\Delta\delta$ = 0.12), and 555 μmole g^{-1} s^{-1} ($\Delta\delta$ = 0.082), at 900 °C and 700 °C, respectively. Table 1 compares the measured peak CO_2 splitting rate and the CO yield with previous studies. The total evolved CO is within the range of reported values, while the peak rates are faster, resulting from the utilization of fine particles and well-controlled experiments which ensure a surface-limited-process.

Kinetics and energy landscape

Model predictions for the CO_2 splitting rates at various temperatures are shown in Fig. 6 for both CeO_2 and $Ce_{0.5}Zr_{0.5}O_2$. The predictions precisely capture the spike-decay behaviors of oxidation, and the non-linear temperature dependence is accurately captured. The kinetics parameters obtained in this study for CeO_2 and $Ce_{0.5}Zr_{0.5}O_2$ are summarized in Table 2.

Fig. 7 shows the calculated energy landscape for the surface chemistry pathways. R1 is exothermic and barrierless, and R2 is endothermic with large activation barriers, indicating that the charge-transfer step (R2) is the rate-limiting step.[28,44] The deep valley connecting the two reaction steps suggests an inverse dependence of CO_3^{2-} concentration on temperature. The CO_2 adsorption/activation energy is found to be −120 kJ $mole^{-1}$ for CZO, half of that with CeO_2, in line with the much lower defect formation energy (see ESI,† Table S1). The following CO desorption energetics, on the other hand, is analogous between the two samples (~160 kJ $mole^{-1}$), although the activation barrier for CZO is noticeably smaller.

Similar values were reported previously based on density functional theory (DFT). Huang and Fabris[46] investigated CO

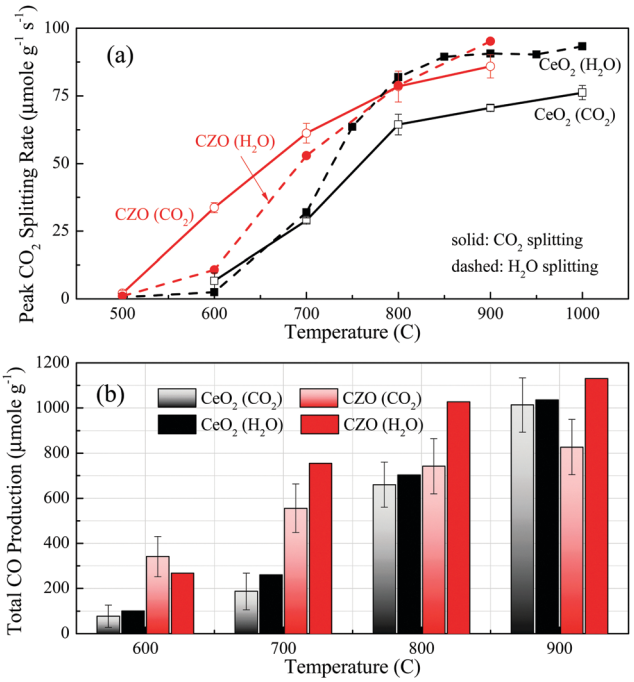

Fig. 5 Comparison of (a) peak splitting rates and (b) total CO production. H_2O splitting results are adopted from ref. 27 and 28. Note the H_2O splitting rates in panel (a) are converted from 26 mol% H_2O to 14.3 mol% H_2O using a linear dependence, as confirmed in ref. 28. Error for the peak rate is based on the s.d. of triplicate peak measurements. Error for total CO production is estimated by multiplying the averaged s.d. of CO measurement by the total oxidation time, which gives an upper bound.

adsorption, (*i.e.*, R2 backward), on a O-bridge site over the stoichiometric ceria (110) surface, and reported −212 kJ $mole^{-1}$ for the adsorption energy, which matches the experimental heat of CO adsorption (−219 kJ $mole^{-1}$) measured by microcalorimetry at 300 °C.[60] Similar values were also reported by Yang *et al.*[51] (−189 kJ $mole^{-1}$), Herschend *et al.*[61] (−205 kJ $mole^{-1}$) and Nolan *et al.*[62] (−188 kJ $mole^{-1}$). The current study of CO_2 splitting with CeO_2 reports a slightly lower CO desorption energy (~160 kJ $mole^{-1}$), likely resulting from a modified structure or energy level of the adsorbed species in the "reverse" (CO_2 oxidation) process, as argued by Cheng *et al.*[37] Their DFT calculations obtained a CO desorption energy of 182 kJ $mole^{-1}$, although the overall splitting process was found to be endothermic because of the lower predicted O-defect formation energy. Yang *et al.*[47] examined the CO_2 desorption process (*i.e.*, R1 backward) following the CO adsorption step using CeO_2 or $Ce_{0.75}Zr_{0.25}O_2$ as the OC, and identified a desorption energy of 245 kJ $mole^{-1}$, and 162 kJ $mole^{-1}$, respectively. These values are in good agreement with those obtained in this study. The formation of CO_3^{2-} *via* CO adsorption was also found to be slightly more favored with CZO, similarly as observed in Fig. 7, which was believed to originate from the more separated excess electrons and hence weaker coulomb repulsion.[47] Nevertheless, the effect is considered to be minor: ~40 kJ $mole^{-1}$ from ref. 47, and ~10 kJ $mole^{-1}$ in this study. The addition of Zr was also found to reduce the CO adsorption barrier,[59] in line with our observation.

The landscape for H_2O splitting is also included for comparison. The energetics of these two processes is generally similar, but subtle differences are associated with the formation of surface adsorbates as well as the charge-transfer step. This similarity can be further examined by comparing the pre-exponential factors, as listed in Table 2. For each material, $k_{1,f}$ and $k_{1,b}$ are almost identical between the H_2O and CO_2 splitting cases, suggesting that the adsorption (R1 forward) or the defect formation (R1 backward) process is highly structure-oriented, and the attempt frequency is mostly controlled by the surface defects, less sensitive to the specific molecular structure of the gaseous oxidizer. R1 differs starkly between CeO_2 and CZO, as the more compact crystal structure with stronger bond energy leads to larger defect formation barrier at a higher vibrational frequency for the R1 backward reaction.[27]

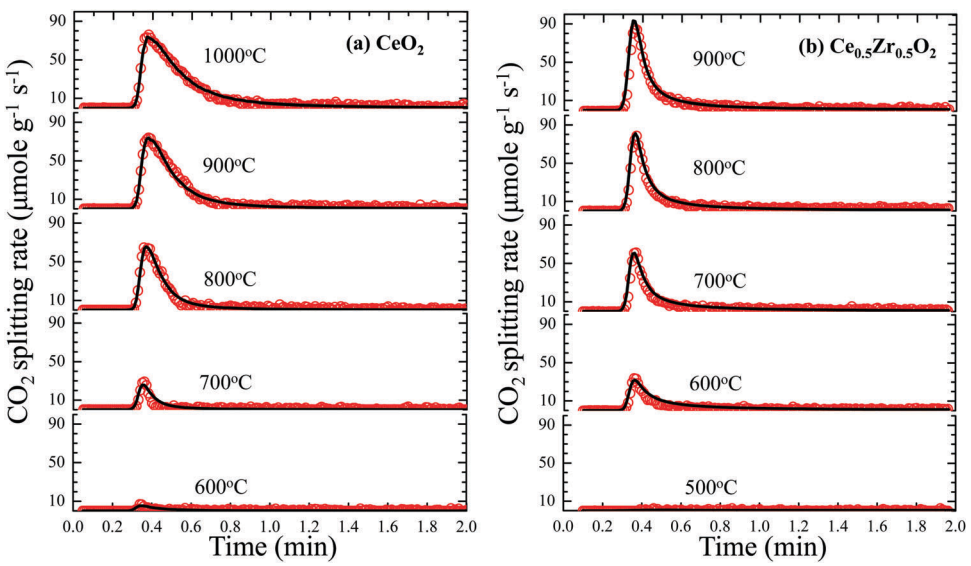

Fig. 6 CO_2 splitting rate for (a) CeO_2 and (b) $Ce_{0.5}Zr_{0.5}O_2$ as a function of temperature. Solid lines represent the defect model. The data sets have been separated to clearly show the comparison.

Table 2 Fitted kinetic parameters for both the forward and backward reactions

	CeO_2 (CO_2)	CZO (CO_2)	CeO_2 (H_2O)[28]	CZO (H_2O)[27]
Adsorption (R1)	$CO_2 + V_O^{\bullet\bullet} + O_O^{\times} \underset{k_{1,b}}{\overset{k_{1,f}}{\rightleftharpoons}} (CO_3)_O^{\bullet\bullet}$		$H_2O + V_O^{\bullet\bullet} + O_O^{\times} \underset{k_{1,b}}{\overset{k_{1,f}}{\rightleftharpoons}} 2OH_O^{\bullet}$	
$k_{1,f}$ (s^{-1})	1.3×10^2	6.4	1.3×10^2	12
$E_{1,f}$ (kJ mol^{-1})	12 ± 10	0 ± 4	7	5
$k_{1,b}$ (s^{-1})	9.4×10^{14}	8.4×10^{11}	8.2×10^{14}	5.0×10^{11}
$E_{1,b}$ (kJ mol^{-1})	251.1 ± 30	120 ± 40	210	92
Charge transfer (R2)	$(CO_3)_O^{\bullet\bullet} + 2Ce'_{Ce} \underset{k_{2,b}}{\overset{k_{2,f}}{\rightleftharpoons}} CO + 2Ce_{Ce}^{\times} + 2O_O^{\times}$		$2OH_O^{\bullet} + 2Ce'_{Ce} \underset{k_{2,b}}{\overset{k_{2,f}}{\rightleftharpoons}} 2O_O^{\times} + 2Ce_{Ce}^{\times} + H_2$	
$k_{2,f}$ (s^{-1})	1.4×10^{13}	1.4×10^{13}	1.5×10^{14}	7.1×10^{14}
$E_{2,f}$ (kJ mol^{-1})	209 ± 40	175 ± 45	190	186
$k_{2,b}$ (s^{-1})	98	16	4.4×10^4	1.0×10^5
$E_{2,b}$ (kJ mol^{-1})	49 ± 4	5 ± 5	97	82

Note: error corresponds to 5% increment of the fitting residual.

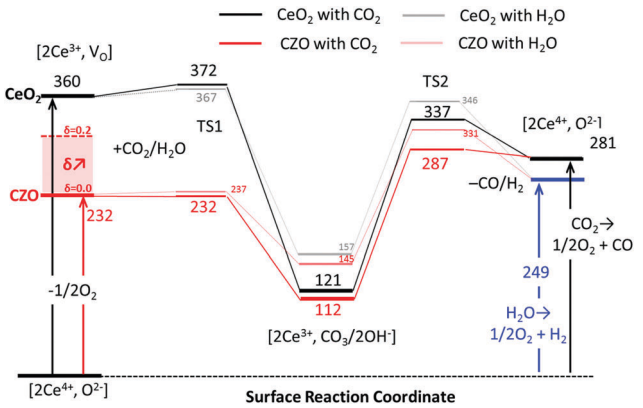

Fig. 7 Energy landscape for the surface reaction pathways for CeO_2 (black) and CZO (red, at stoichiometry). The pathways for H_2O splitting are also included (gray and light red) for comparison. Unit is kJ $mole^{-1}$. The increase of defect formation enthalpy with non-stoichiometry for CZO, detailed in ESI,† is also included.

The higher $k_{1,f}$ for CeO_2 may be related to the higher defect concentrations (see Fig. 3) and more favorable adsorption sites. The calculated $k_{1,b}$'s are within the range of vibrational frequencies reported for oxides.[57,63,64]

On the other hand, the charge-transfer process (R2) is similar for both CeO_2 and CZO with the same oxidizer. This is expected, given the fact that the charge-transfer step mostly depends on the evolution of the surface adsorbates and the interactions with the lattice oxygen, and is less affected by the structural relaxation effect from Zr. $k_{2,f}$ can be estimated based on the vibrational frequency of the adsorbates,[28,57] *i.e.*, ν_0 (CO_3^{2-}) = 1.5×10^{13}–5×10^{13},[47,62,64,65] and $\nu_0(OH^-) = 1 \times 10^{14}$ s^{-1}.[64,66] The estimated attempt frequency is a good match with $k_{2,f}$ derived from kinetics fitting. The much higher $k_{2,b}$ in the H_2O cases may be attributed to the much faster collision frequency of H_2 with more preferable adsorption sites and orientations as compared to CO.

To further examine the rate-limiting mechanism, the calculated forward and the backward reaction rates and the evolution of the surface carbonate concentration are shown in Fig. 8. The CO_2 activation step (R1) is faster in all cases, and equilibrium is quickly established between the surface carbonates and the gaseous CO_2. The charge transfer step (R2) is slower, especially at low temperature, and the backward reaction is close to zero, showing that the charge transfer process is the rate-limiting step, as observed for CO_2 splitting with Sm-doped ceria[44] as well as in the H_2O splitting processes.[27,28,56] The derived activation barriers (*i.e.* 209 kJ $mole^{-1}$ for CeO_2 and 175 kJ $mole^{-1}$ for CZO) for the rate-limiting step possibly correspond to the range of the apparent activation energy, 120–200 kJ $mole^{-1}$, from the previously reported empirical models.[17] Compared to CZO, the rates of R1 at 900 °C with CeO_2 are faster initially followed by a rapid decay, in accordance with the evolution of the surface defects, as shown in Fig. 3. In contrast, the rates with CZO at 700 °C are consistently higher, owing to the higher surface area and the larger oxygen non-stoichiometry established after reduction. The rates of R1 forward with CZO are almost the same between 900 °C and 700 °C, resulting from negligible $E_{1,f}$ and a similar surface defect concentration (see Fig. 4(d)). The similarity of R1 backward is a combined effect from $E_{1,b}$ and the reverse temperature dependence of CO_3^{2-}, as shown in panels (b) and (d). CO_3^{2-} concentration with CeO_2 is higher and more temperature sensitive, which agrees with the deeper valley as plotted in Fig. 7.

Surface adsorbates and ion-exchange dynamics

The surface absorbates act as a buffer to mediate the differences in reaction rate kinetics of the adsorption process and the following charge-transfer step, and their formation and evolution critically rely on the surface defect structure. To understand the correlation between the surface defects and the adsorbates and their roles in CO_2/H_2O splitting, we examine the out-of-equilibrium dynamics of Ce^{3+} and CO_3^{2-} in response to the ion-incorporation flux, J, by equating eqn (5) and (7) as:

$$\begin{aligned} J &= k_{1,f} p_{CO_2} \left[V_O^{\bullet\bullet}\right]\left[O_O^{\times}\right] - k_{1,b}\left[CO_3^{2-}\right] \\ &= k_{2,f}\left[CO_3^{2-}\right]\left[Ce'_{Ce}\right]^2 - k_{2,b} p_{CO}\left[O_O^{\times}\right]^2\left[Ce_{Ce}\right]^2 \end{aligned} \quad (12)$$

Eqn (12) essentially represents the majority of the conversion process where $d[CO_3^{2-}]/dt \approx 0$ (see ESI†), as seen in Fig. 8, with the only exception at the onset of oxidizer flow. J is positive in

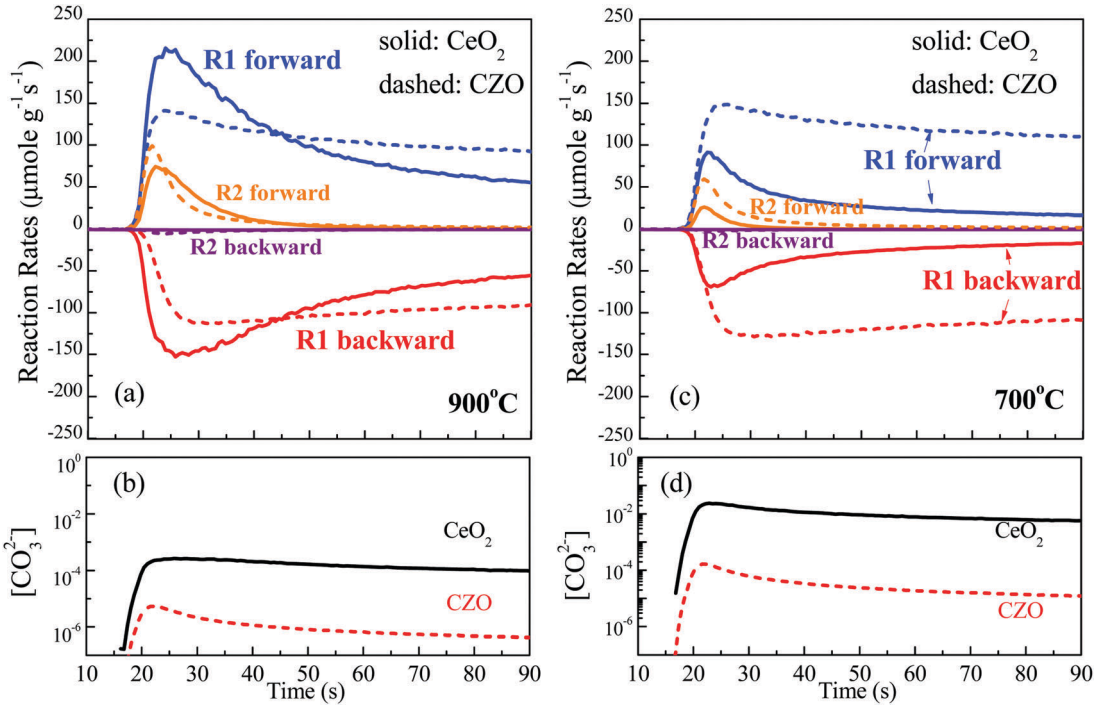

Fig. 8 Comparison of the surface reaction rates and surface carbonate concentrations at 900 °C and 700 °C for CeO_2 (solid lines) and CZO (dashed lines). Backward reactions are plotted as negative values for clarity.

oxidation and negative in reduction. By re-arranging eqn (12), J and $[CO_3^{2-}]$ are expressed as:

$$J = \frac{k_{1,f}k_{2,f}p_{CO_2}\left[V_O^{\bullet\bullet}\right]\left[O_O^{\times}\right]\left[Ce'_{Ce}\right]^2 - k_{1,b}k_{2,b}p_{CO}\left[O_O^{\times}\right]^2[Ce_{Ce}]^2}{k_{2,f}\left[Ce'_{Ce}\right]^2 + k_{1,b}} \quad (13)$$

$$[CO_3^{2-}] = \frac{k_{1,f}p_{CO_2}\left[V_O^{\bullet\bullet}\right]\left[O_O^{\times}\right] + k_{2,b}p_{CO}\left[O_O^{\times}\right]^2[Ce_{Ce}]^2}{k_{2,f}\left[Ce'_{Ce}\right]^2 + k_{1,b}} \quad (14)$$

The numerator in eqn (13) is the off-equilibrium (*i.e.*, biasing) potential, and the denominator describes the resistances to the generation of fluxes from both redox directions (*i.e.*, $k_{2,f}\left[Ce'_{Ce}\right]^2$ is the charge transfer resistance for the oxidation step, and $k_{1,b}$ is the defect formation resistance for reduction). Therefore, eqn (13) essentially describes the electro-chemical processes in solid-oxide electrode cells for CO_2 splitting, in which the ion flux controlled by the over-potential and J represents the current density, as in ref. 44 and 56. The concentrations of Ce^{3+} and CO_3^{2-} are solved with varying J, and the correlations in a typical oxidizing environment (CO_2 = 0.14 bar, and CO = 0.02 bar) are shown in Fig. 9.

As seen in panel (a), CO_3^{2-} concentration with CeO_2 rises linearly with Ce^{3+} initially, flattens when half of the surface is reduced, and eventually starts to decrease as the surface is near completely reduced. This originates from a mismatch of the kinetic rates between R1 and R2. At low $[Ce^{3+}]$, the charge-transfer reaction (R2) is slow, and CO_3^{2-} concentration is solely determined by R1: eqn (14) becomes $[CO_3^{2-}] \approx K_1 p_{CO_2}\left[V_O^{\bullet\bullet}\right]\left[O_O^{\times}\right]$, thus exhibiting a linear dependence. With the increase of $[Ce^{3+}]$, R2 becomes more pronounced following a parabolic dependence. The rapid consumption *via* R2 slows down the accumulation of CO_3^{2-} *via* R1, leading to the observed transition. In this stage, the dependence of CO_3^{2-} can be approximated as $[CO_3^{2-}] \sim [Ce^{3+}]/(1 + A_0[Ce^{3+}]^2)$. Similar phenomena were reported by Chueh and co-workers[44] when the surface of the $Sm_{0.2}Ce_{0.8}O_{1.9}$ electrode was examined using ambient pressure X-ray photoelectron spectroscopy in a CO_2 oxidizing environment at 500 °C. They attributed this observation to the carbonate coverage effect, and argued that the adsorbate–adsorbate interaction modifies the adsorption and charge transfer electrochemistry, hence leading to the varying dependence. Our analysis shows that this phenomenon can simply be explained in terms of the mismatch in the kinetic rates of R1 and R2. The surface carbonate coverage reaches a maximum of ~3% at 700 °C, but is significantly lower (~0.03%) at 900 °C, in line with the deep valley in the energy roadmap (Fig. 7). $[CO_3^{2-}]$ at 500 °C is calculated to be around 10–30%, in reasonable agreement with the estimation (~20%) from ref. 44.

The evolution of OH^- during the H_2O splitting process is also included in panel (a) for comparison. In contrast to the pattern of CO_3^{2-}, the $[OH^-]$ curve is concave and increases mildly with Ce^{3+} without a linear initial stage. A similar pattern was also identified by Chueh and co-workers.[56] This behavior is related to the fact that two OH^- adsorbates are involved in R1 or R2 (see Table 2). Consequently, $[OH^-] \sim \sqrt{[Ce^{3+}]}$ at the early stage, and then transits to $[OH^-] \sim \sqrt{[Ce^{3+}]}\Big/\sqrt{1 + A_0[Ce^{3+}]^2}$. The temperature dependence is weaker, owing to the slightly higher energy level associated with OH^- as shown in Fig. 7.

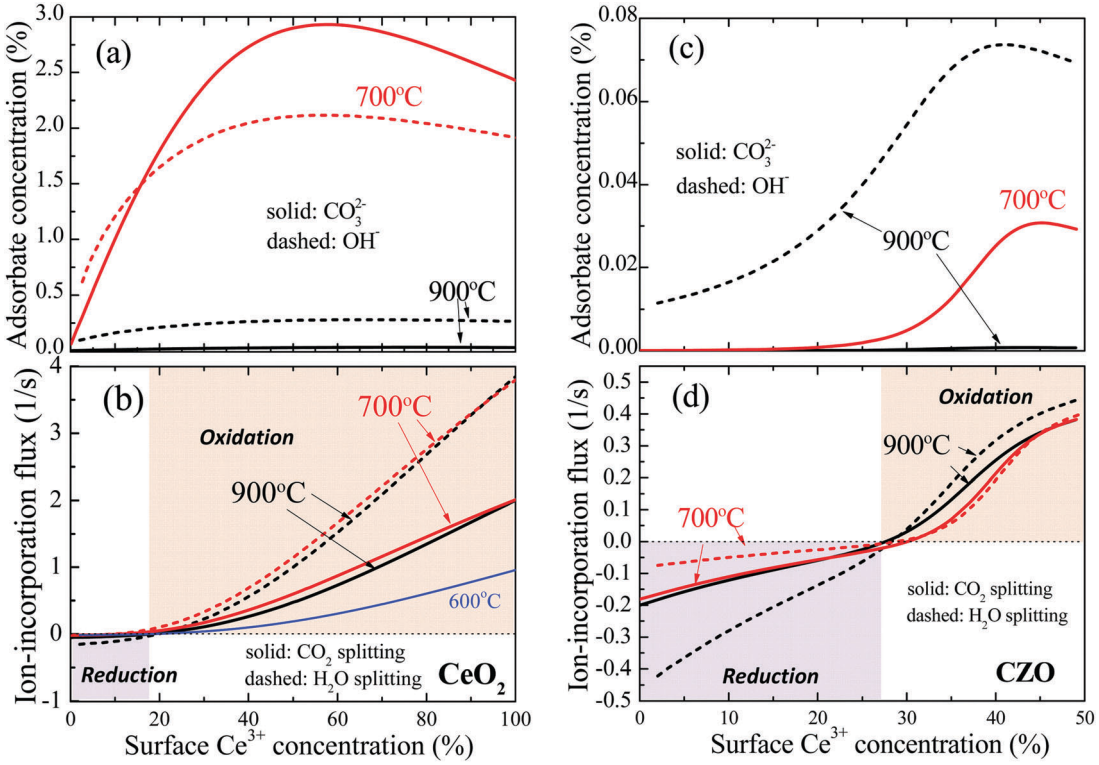

Fig. 9 Calculated evolutions of the concentration of surface adsorbates (panels a, c), and ion-incorporation flux (panels b, d) as a function of the surface Ce^{3+} concentration at 900 °C (black) and 700 °C (red). The results with H_2O splitting (dashed lines, OH^- as adsorbate) are also included with surface chemistry from ref. 27 and 28 and the kinetic parameters are summarized in Table 2. CO_2 or H_2O is fixed at 0.14 bar, and CO or H_2 is 0.02 bar, which represents a typical environment in oxidation. Filled areas in panel b, or d correspond to oxidation, *i.e.*, a positive flux, and reduction, *i.e.*, a negative flux. Panels a, b are for CeO_2, and panels c, d are for CZO.

The correlation between the ion-incorporation flux, J, and the surface Ce^{3+} concentration is shown in panel (b). In an oxidizing environment, *i.e.*, CO_2 = 0.14 bar, and CO = 0.02 bar, the ion flux is mostly positive, except at very low Ce^{3+} where the removal of surface oxygen *via* R2 backward becomes significant. Interestingly, the flux curve exhibits a very weak temperature dependence, because of roughly the same temperature dependence for the numerator and the denominator in eqn (13). Despite the observed similarity in the ion-incorporation fluxes, the surface defects created in the preceding reduction step critically depends on temperature, which results in the observed dependence of splitting kinetics on temperature. Consequently, the splitting peak rate increases significantly around 700 °C, but becomes overlapped at a further elevated temperature (see Fig. 4), in accordance with the similar trend of Ce^{3+} at the surface. It is worth noting that a further decrease in temperature, however, leads to a much reduced flux, (*e.g.* blue line in panel b), because the carbonate saturates on the surface, hence reducing the concentration of $V_O^{\bullet\bullet}$ and $O_O^{\times}$. Compared to CO_2 splitting, H_2O oxidation with CeO_2 is noticeably faster, as also evident in Fig. 5(a).

Compared to CeO_2, the concentration of CO_3^{2-} on the CZO surface is much lower and its evolution starts with an exponential rise, followed by a slight decrease when all available Ce^{4+} is reduced to Ce^{3+}, as seen in panel (c). This is related to the positive δ dependence of $E_{1,b}$ as stated in the ESI.† Consequently, $k_{1,b}$ in the denominator of eqn (14) decays with the creation of the oxygen vacancy, thus leading to the observed exponential increase of CO_3^{2-} with Ce^{3+}. This effect becomes less prominent at high concentration of Ce^{3+} when the first term in the denominator, $k_{2,f}\left[Ce'_{Ce}\right]^2$, becomes comparable with $k_{1,b}$. OH^- concentration is conceivably higher compared to CO_3^{2-} at all temperatures, again echoing the deeper valley as seen in Fig. 7. As shown in panel (d), the ion-incorporation flux exhibits different patterns as compared to CeO_2. The range of reduction with negative J is significantly expanded, resulting from the much improved reducibility of CZO. As a result, oxygen removal is favored as the concentration of Ce^{3+} is below 25%, even under a highly oxidizing environment.

Compared to CO_2 splitting, oxidation with H_2O is noticeably faster at 900 °C, but becomes slower at 700 °C although the difference is minor. The comparison of the flux here is in good accordance with the observation in Fig. 5(a). The surface Ce^{3+} concentration at equilibrium, *i.e.*, J = 0, is in fact very similar between the two cases, although the H_2O splitting process equilibrates at a slightly higher Ce^{3+} (thus with a higher equilibrium p_{O_2}) compared to CO_2 splitting at 900 °C, and it becomes slightly lower at 700 °C. This comparison supports the speculation that the observed difference in the CO/H_2 yield in Fig. 5(b) is kinetics-related, originating from the weaker temperature dependence of CO_2 splitting kinetics.

Conclusion

This work presents a detailed kinetics study of CO_2 splitting using CeO_2 and $Ce_{0.5}Zr_{0.5}O_2$ nano-powder. The time-resolved kinetics are measured in a button cell reactor in the temperature range 600–900 °C at atmospheric pressure. The ceria-based sample is alternatively exposed to the H_2/Ar mixture in the reduction cycle to remove the lattice oxygen, and CO_2 in the oxidation cycle to produce CO. Evident improvement is found for CZO at lower temperatures with twice as fast kinetics at 700 °C, resulting from the enhanced reducibility with Zr and the finer particle structures maintained throughout the redox cycling. The peak rates with CZO are 85.9 μmole g^{-1} s^{-1} at 900 °C and 61.2 μmole g^{-1} s^{-1} at 700 °C, and those of CeO_2 are 70.6 μmole g^{-1} s^{-1} and 28.9 μmole g^{-1} s^{-1}.

Kinetics models are developed to describe the ion incorporation dynamics, with consideration of two-step chemistry: CO_2 activation over surface defects followed by the charge transfer process. Excellent agreement of the model with the fitted parameters is achieved compared to the measurements. The CO_2 activation energy is found to be −120 kJ $mole^{-1}$ for CZO, half of that with CeO_2, while the following CO desorption energetics is analogous between the two samples with a value of ∼160 kJ $mole^{-1}$, with a weaker activation barrier for CZO. The derived reaction roadmap and energetics are analogous with the H_2O splitting kinetics, with the difference mostly in the formation of surface adsorbates and the following charge-transfer process. The CO_2 activation process differs starkly between CeO_2 and CZO, due to the different defect formation thermodynamics.

The charge-transfer process is found to be the rate-limiting step for CO_2 splitting. With the derived kinetics, the evolution of the adsorbates with surface Ce^{3+} is examined, and a linear-flattened-decay pattern is observed for CeO_2, resulting from mismatch of the rate kinetics of the two reactions. The formation of carbonate is found to be reversely temperature dependence, reaching 3% at 700 °C. Compared to CeO_2, the concentration of CO_3^{2-} on CZO surface is much lower and it evolves more non-linearly with surface Ce^{3+}. The kinetics study here unveils the significant role of the surface defects and their interactions with adsorbates in determining the splitting kinetics.

Conflicts of interest

There are no conflicts to declare.

Acknowledgements

This study is financially supported by a grant from British Petroleum (BP) and the King Abdullah University of Science and Technology (KAUST) Investigator Award.

References

1 S. Abanades and G. Flamant, *Sol. Energy*, 2006, **80**, 1611–1623.
2 W. C. Chueh, C. Falter, M. Abbott, D. Scipio, P. Furler, S. M. Haile and A. Steinfeld, *Science*, 2010, **330**, 1797–1801.
3 P. Furler, J. Scheffe, M. Gorbar, L. Moes, U. Vogt and A. Steinfeld, *Energy Fuels*, 2012, **26**, 7051–7059.
4 P. Furler, J. R. Scheffe and A. Steinfeld, *Energy Environ. Sci.*, 2012, **5**, 6098–6103.
5 S. Abanades and M. Chambon, *Energy Fuels*, 2010, **24**, 6667–6674.
6 A. Stamatiou, P. Loutzenhiser and A. Steinfeld, *Chem. Mater.*, 2009, **22**, 851–859.
7 T. Montini, M. Melchionna, M. Monai and P. Fornasiero, *Chem. Rev.*, 2016, **116**, 5987–6041.
8 M. Mogensen, N. M. Sammes and G. A. Tompsett, *Solid State Ionics*, 2000, **129**, 63–94.
9 R. Panlener, R. Blumenthal and J. Garnier, *J. Phys. Chem. Solids*, 1975, **36**, 1213–1222.
10 H. Tuller and A. Nowick, *J. Electrochem. Soc.*, 1979, **126**, 209–217.
11 A. Le Gal, S. Abanades and G. Flamant, *Energy Fuels*, 2011, **25**, 4836–4845.
12 S. Abanades and A. Le Gal, *Fuel*, 2012, **102**, 180–186.
13 S. G. Rudisill, L. J. Venstrom, N. D. Petkovich, T. Quan, N. Hein, D. B. Boman, J. H. Davidson and A. Stein, *J. Phys. Chem. C*, 2013, **117**, 1692–1700.
14 P. Furler, J. Scheffe, D. Marxer, M. Gorbar, A. Bonk, U. Vogt and A. Steinfeld, *Phys. Chem. Chem. Phys.*, 2014, **16**, 10503–10511.
15 Q. Jiang, G. Zhou, Z. Jiang and C. Li, *Sol. Energy*, 2014, **99**, 55–66.
16 B. Zhao, C. Huang, R. Ran, X. Wu and D. Weng, *J. Mater. Sci.*, 2016, **51**, 2299–2306.
17 S. Ackermann, L. Sauvin, R. Castiglioni, J. L. M. Rupp, J. R. Scheffe and A. Steinfeld, *J. Phys. Chem. C*, 2015, **119**, 16452–16461.
18 L. J. Venstrom, N. Petkovich, S. Rudisill, A. Stein and J. H. Davidson, *J. Sol. Energy Eng.*, 2012, **134**, 011005.
19 L. J. Venstrom, R. M. De Smith, Y. Hao, S. M. Haile and J. H. Davidson, *Energy Fuels*, 2014, **28**, 2732–2742.
20 J. Kašpar, P. Fornasiero and M. Graziani, *Catal. Today*, 1999, **50**, 285–298.
21 J. R. Scheffe, R. Jacot, G. R. Patzke and A. Steinfeld, *J. Phys. Chem. C*, 2013, **117**, 24104–24114.
22 A. Trovarelli, M. Boaro, E. Rocchini, C. de Leitenburg and G. Dolcetti, *J. Alloys Compd.*, 2001, **323**, 584–591.
23 P. Fornasiero, R. Dimonte, G. R. Rao, J. Kaspar, S. Meriani, A. Trovarelli and M. Graziani, *J. Catal.*, 1995, **151**, 168–177.
24 G. Balducci, M. S. Islam, J. Kašpar, P. Fornasiero and M. Graziani, *Chem. Mater.*, 2000, **12**, 677–681.
25 K. Ahn, H. He, J. M. Vohs and R. J. Gorte, *Electrochem. Solid-State Lett.*, 2005, **8**, A414–A417.
26 R. Di Monte and J. Kašpar, *Top. Catal.*, 2004, **28**, 47–57.
27 Z. Zhao, M. Uddi, N. Tsvetkov, B. Yildiz and A. F. Ghoniem, *J. Phys. Chem. C*, 2017, **121**, 11055–11068.
28 Z. Zhao, M. Uddi, N. Tsvetkov, B. Yildiz and A. F. Ghoniem, *J. Phys. Chem. C*, 2016, **120**, 16271–16289.
29 A. Trovarelli, *Catal. Rev.*, 1996, **38**, 439–520.
30 R. Di Monte and J. Kašpar, *Catal. Today*, 2005, **100**, 27–35.
31 S. Pengpanich, V. Meeyoo, T. Rirksomboon and K. Bunyakiat, *Appl. Catal., A*, 2002, **234**, 221–233.
32 H. Yao and Y. Y. Yao, *J. Catal.*, 1984, **86**, 254–265.

33 H. Cordatos and R. Gorte, *J. Catal.*, 1996, **159**, 112–118.
34 C. Li, Y. Sakata, T. Arai, K. Domen, K.-i. Maruya and T. Onishi, *J. Chem. Soc., Faraday Trans. 1*, 1989, **85**, 929–943.
35 R. J. Gorte, *AIChE J.*, 2010, **56**, 1126–1135.
36 S. H. Oh and C. C. Eickel, *J. Catal.*, 1988, **112**, 543–555.
37 Z. Cheng, B. J. Sherman and C. S. Lo, *J. Chem. Phys.*, 2013, **138**, 014702.
38 W. C. Chueh, A. H. McDaniel, M. E. Grass, Y. Hao, N. Jabeen, Z. Liu, S. M. Haile, K. F. McCarty, H. Bluhm and F. El Gabaly, *Chem. Mater.*, 2012, **24**, 1876–1882.
39 G. Zhou, P. R. Shah, T. Montini, P. Fornasiero and R. J. Gorte, *Surf. Sci.*, 2007, **601**, 2512–2519.
40 J. Paier, C. Penschke and J. Sauer, *Chem. Rev.*, 2013, **113**, 3949–3985.
41 T. Staudt, Y. Lykhach, N. Tsud, T. Skala, K. Prince, V. Matolín and J. Libuda, *J. Catal.*, 2010, **275**, 181–185.
42 S. Sharma, S. Hilaire, J. Vohs, R. Gorte and H.-W. Jen, *J. Catal.*, 2000, **190**, 199–204.
43 M. Rothensteiner, S. Sala, A. Bonk, U. Vogt, H. Emerich and J. A. van Bokhoven, *Phys. Chem. Chem. Phys.*, 2015, **17**, 26988–26996.
44 Z. A. Feng, M. L. Machala and W. C. Chueh, *Phys. Chem. Chem. Phys.*, 2015, **17**, 12273–12281.
45 Y. Lykhach, T. Staudt, R. Streber, M. Lorenz, A. Bayer, H.-P. Steinrück and J. Libuda, *Eur. Phys. J. B*, 2010, **75**, 89–100.
46 M. Huang and S. Fabris, *J. Phys. Chem. C*, 2008, **112**, 8643–8648.
47 Z. Yang, Z. Fu, Y. Wei and Z. Lu, *J. Phys. Chem. C*, 2008, **112**, 15341–15347.
48 K. R. Hahn, M. Iannuzzi, A. P. Seitsonen and J. r. Hutter, *J. Phys. Chem. C*, 2013, **117**, 1701–1711.
49 L. J. Venstrom, R. M. De Smith, R. Bala Chandran, D. B. Boman, P. T. Krenzke and J. H. Davidson, *Energy Fuels*, 2015, **29**, 8168–8177.
50 Z. Zhao, PhD dissertation, Massachusetts Institute of Technology, 2016.
51 Z. Yang, T. K. Woo and K. Hermansson, *Chem. Phys. Lett.*, 2004, **396**, 384–392.
52 M. Nolan and G. W. Watson, *J. Phys. Chem. B*, 2006, **110**, 16600–16606.
53 V. Shapovalov and H. Metiu, *J. Catal.*, 2007, **245**, 205–214.
54 D. O. Scanlon, N. M. Galea, B. J. Morgan and G. W. Watson, *J. Phys. Chem. C*, 2009, **113**, 11095–11103.
55 Y. Yu, B. Mao, A. Geller, R. Chang, K. Gaskell, Z. Liu and B. W. Eichhorn, *Phys. Chem. Chem. Phys.*, 2014, **16**, 11633–11639.
56 Z. A. Feng, F. El Gabaly, X. Ye, Z.-X. Shen and W. C. Chueh, *Nat. Commun.*, 2014, **5**, 4374.
57 D. Marrocchelli and B. Yildiz, *J. Phys. Chem. C*, 2012, **116**, 2411–2424.
58 H. A. Hansen and C. Wolverton, *J. Phys. Chem. C*, 2014, **118**, 27402–27414.
59 Z. Yang, Z. Fu, Y. Zhang and R. Wu, *Catal. Lett.*, 2011, **141**, 78–82.
60 M. Breysse, M. Guenin, B. Claudel and J. Veron, *J. Catal.*, 1973, **28**, 54–62.
61 B. Herschend, M. Baudin and K. Hermansson, *Chem. Phys.*, 2006, **328**, 345–353.
62 M. Nolan, S. C. Parker and G. W. Watson, *Surf. Sci.*, 2006, **600**, 175–178.
63 A. Kushima and B. Yildiz, *J. Mater. Chem.*, 2010, **20**, 4809–4819.
64 C. Binet, M. Daturi and J.-C. Lavalley, *Catal. Today*, 1999, **50**, 207–225.
65 *NIST Standard Reference Database Number 101. Release 17b*, September 2015, ed. R. D. Johnson III. http://cccbdb.nist.gov/.
66 K.-P. Huber, *Molecular spectra and molecular structure: IV. Constants of diatomic molecules*, Springer Science & Business Media, 2013.